Materials Today Bio 32 (2025) 101730

Contents lists available at ScienceDirect

Materials Today Bio

journal homepage: www.journals.elsevier.com/materials-today-bio

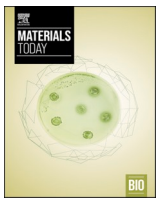

Bioactive deproteinized bovine bone mineral based on self-assembled albumin nanoparticles promoted bone regeneration via activation of Wnt/β-catenin pathway

Ya-wen Zhu [a,b], Yu-wen Wei [a,b], Jing-yi Ma [a,b], Wei Chen [a,b], Zhe Shen [a,b], Jing Qiu [a,b,c,*]

[a] Department of Oral Implantology, Affiliated Stomatological Hospital of Nanjing Medical University, Nanjing, China
[b] Jiangsu Province Key Laboratory of Oral Diseases, Nanjing, China
[c] Jiangsu Province Engineering Research Center of Stomatological Translational Medicine, Nanjing, China

ARTICLE INFO

Keywords:
TD-BNP@DBBM
Wnt/β-catenin
Osteogenesis
Bone regeneration

ABSTRACT

One of the major problems faced with pre-implant bone reconstruction therapy is that large bone defects do not heal over time. Artificial bone graft materials, such as deproteinized bovine bone mineral, are commonly used in clinics. However, the lack of osteoinductive capacity and risk of post-implantation infections remain key limitations. Bioactive materials with strong bone formation and a high degree of biocompatibility are still needed. In this study, we synthesised bovine serum albumin nanoparticles (BNP) loaded with Tideglusib (TD), TD and BNP were bound together by self-assembly, and mixed with deproteinized bovine bone mineral (DBBM) to form a bone substitute material (TD-BNP@DBBM) that had low cytotoxicity, promoted cell proliferation and migration, induced cell differentiation, and regulated osteogenesis. In vitro, experiments suggested that TD-BNP@DBBM could promote osteoblast differentiation of MC3T3-E1 cells. In vivo, experiments demonstrated that TD-BNP@DBBM significantly accelerated bone reconstruction and enhanced bone healing in a rat cranial defect model. Furthermore, this result suggested a link between the Wnt/β-catenin pathway and the osteogenic effect, providing a basis for subsequent investigations into the mechanism of bone regeneration induced by osteogenic biomaterials. TD-BNP@DBBM might be a promising new approach for treating bone defects.

1. Introduction

The reconstruction of bone defects, particularly those of a critical size where spontaneous osseointegration is not feasible without surgical intervention, represents a significant challenge in preimplantation bone reconstruction [1–4]. The feasibility of regenerating clinical bone defects using autologous and allogeneic transplants is constrained by donor scarcity and strong immunogenicity [5]. Using biologically engineered bone regeneration materials that imitate the natural extracellular matrix, facilitate cell-matrix signalling, and regulate biomineralisation and osseointegration may provide a substitute solution to this problem. For instance, collagen [6], deproteinized bovine bone mineral (DBBM) [7,8], and other similar substances have been further developed as replaceable bone grafts to regenerate bone defects effectively [9–12]. However, there are still limitations in the osteogenic capacity of these bionic scaffolds, they have only osteoconductive effects, while the usage of bone morphogenetic protein 2 (BMP-2) [13–15], which has osteoinductive effects, is currently limited due to its high price. In the last decade, natural products in the field of osteogenic material, especially small molecule compounds such as flavonoids [16–18], have received more and more attention in engineering. Clinically, few treatments are available for systemic or oral administration due to a lack of bone defect site distribution or insufficient capacity. Local delivery via biomaterial implants effectively promotes new bone formation as an alternative to systemic delivery [19–21].

Tideglusib, a small molecule chemically synthesised drug, was initially developed to treat Alzheimer's disease [22]. TD has the advantages of not requiring the extraction of a patient's blood, easy preservation, and low cost, it has a promising application in inducing bone regeneration. It has been shown that the use of degradable gelatin sponges as a vehicle to stimulate restorative dentin formation by mobilising pulp stem cells, and gradually replacing degraded gelatin

* Corresponding author. Affiliated Stomatological Hospital of Nanjing Medical University, 1# Shanghai Road, Nanjing, 210029, China.
E-mail address: qiujing@njmu.edu.cn (J. Qiu).

https://doi.org/10.1016/j.mtbio.2025.101730
Received 13 November 2024; Received in revised form 29 March 2025; Accepted 4 April 2025
Available online 4 April 2025

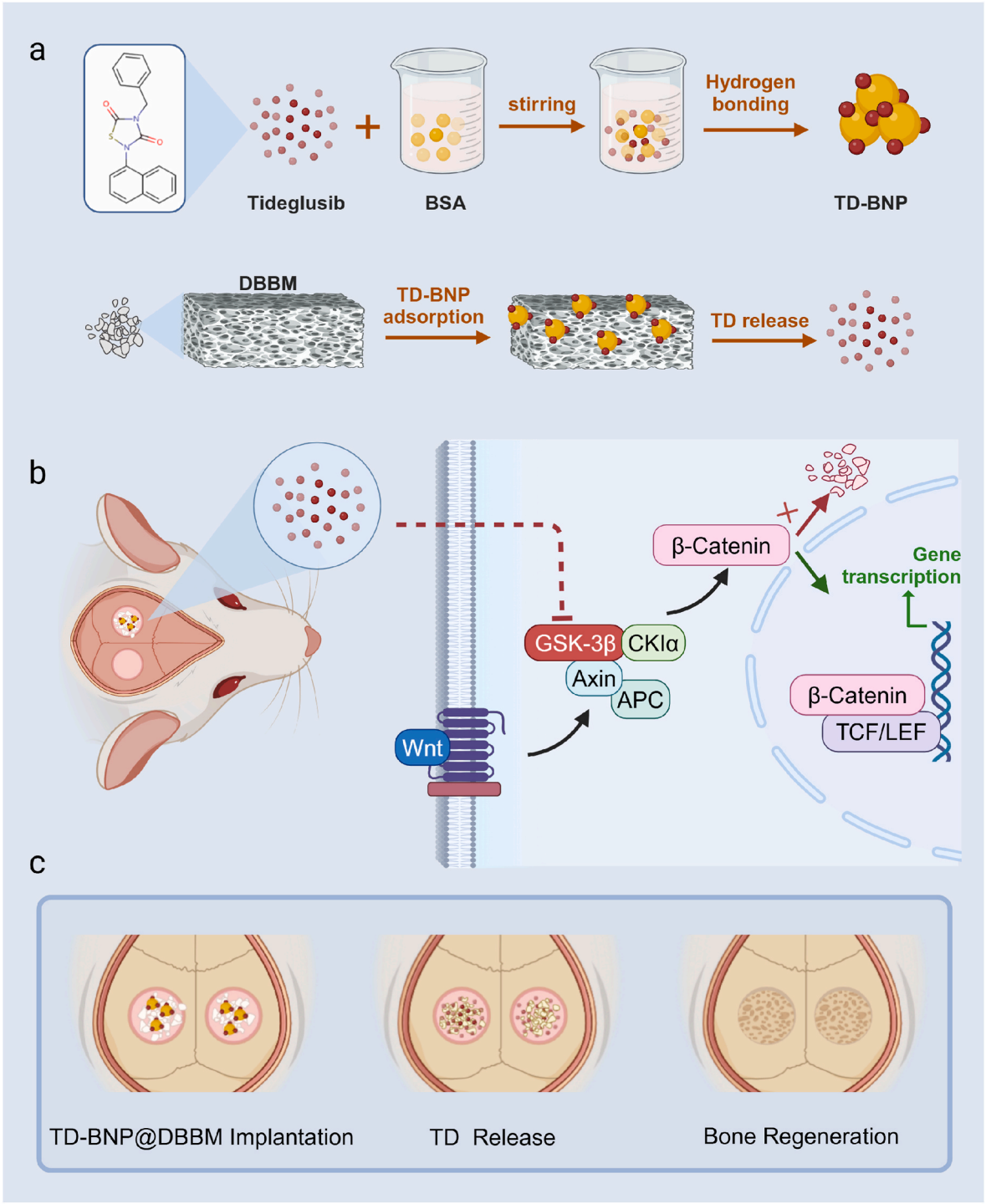

Fig. 1. Schematic illustration of TD-BNP@DBBM preparation and schematic diagram of its application in treating critical-size cranial defects. (a) Preparation process of TD-BNP@DBBM. (Arrows represent processes, TD-BNP: BSA nanoparticles loaded with tideglusib, TD-BNP@DBBM: TD-BNP loading onto deproteinized bovine bone mineral,TD release: tideglusib release from TD-BNP@DBBM). (b) Mechanism of TD-BNP@DBBM in promoting bone regeneration. (c) Schematic diagram of TD-BNP@DBBM applied to repair of critical bone defects in rats.

sponges to achieve complete and adequate natural dentin restoration may provide a new clinical solution for the repair of dental defects [23–25]. According to molecular docking technology, TD has a high affinity for GSK-3β. The induction of osteogenic differentiation might be through the Wnt/β-catenin pathway, which is the critical event mediating bone repair.

Bovine serum albumin (BSA) is structurally similar to human serum albumin (HSA) [26], which is a widely used biochemical reagent in many disciplines of biology and various fields of medicine. The presence of abundant amino acid residues and free sulfhydryl groups and the presence of a large number of disulphide bonds in BSA results in a wide range of binding capabilities to a variety of anions and cations and other small molecules [26–28].

Given the excellent biocompatibility of BSA, BSA nanoparticles were synthesised in the present study. BSA nanoparticles have a good release function for sustained drug release. The nanoparticle system can be used

to control the rate and mode of drug release and reduce the frequent administration of drugs [29–31]. To maximise the effect of the drug, we proposed a local drug delivery method to achieve local release and slow release of Tideglusib by preparing TD-BNP nanoparticles.

Studies have shown that Tideglusib is an antagonist of GSK-3β, an essential downstream component of the Wnt/β-catenin pathway [32]. To further investigate the mechanisms associated with TD-BNP and osteogenic differentiation, the present study hypothesised that TD-BNP inhibits the GSK-3β by releasing the Tideglusib, then activating the pathway, and providing a new idea for clinical bone biomaterials through the joint action of TD-BNP and deproteinized bovine bone mineral (DBBM) (Fig. 1).

2. Materials and methods

2.1. Materials

Tideglusib, MASB and Bovine serum albumin were purchased from MedChemExpress (USA), and deproteinized bovine bone mineral (DBBM) was purchased from Geistlich (Switzerland). Live/dead staining kit, Cell Counting Kit 8 reagent, rhodamine-ghost pen cyclic peptide, DAPI, crystal violet, ALP staining kit, radioimmunoprecipitation assay buffer, alizarin red staining, BCA Protein Assay Kit, 0.1 % Triton X-100, Enhanced chemiluminescence reagent were purchased from Beyotime (China). Trizol reagent was purchased from Thermo Fisher Scientific (USA). PVDF membranes were purchased from Millipore (USA). The SYBR Green MasterSupermix kit was purchased in Takara (Japan).

2.2. Preparation of TD-BNP

First, BSA (10, 20, 30, 40 mg/mL) and TD (1 mg/mL) were added to the 10 mL vessel, and pH was titrated to 9 by adding NaOH solution (0.01 M). Anhydrous ethanol solution was added at a speed of 2 mL/min, and the reaction was completed after 12 h of stirring. The TD-BNP were dialysed and purified (1 L/dose) for 24 h. Then, they were centrifuged at 10000 rpm for 5 min, and TD-BNP were stored at −4 °C for further use.

2.3. Characterization of TD-BNP

TD-BNP was captured utilising SEM (Zeiss, Germany) at two magnifications (1 μm, 500 nm) at an elevated voltage of 20 kV. Subsequently, TEM (Tecnai, FEI, USA) was employed to elucidate the internal structure of the TD-BNP at two different magnifications (500 nm and 50 nm). FT-IR (iS10, Nicolet, USA) was used to examine the nanoparticles' chemical structure. DLS (Nano-ZS 90, Malvern, UK) evaluated the nanoparticle size distribution and zeta potential.

2.4. Release assay of TD-BNP

Standard curves were obtained by measuring different concentrations of TD using a UV spectrophotometer (UV-8000, Metasch, China), and the encapsulation rate of TD was measured at different mass ratios (BSA: TD). To determine the release of TD at a mass ratio of 20:1 using the UV spectrophotometer (UV-8000, Metasch, China), TD-BNP was immersed in 3 mL of PBS and incubated in the shaker. At the indicated time points, 1 mL of supernatant was aspirated and centrifuged, and 1 mL of fresh PBS was added. A UV spectrophotometer (UV-8000, Metasch, China) was then used to measure the amount of TD that was released by TD-BNP from the supernatant.

2.5. Molecular dynamics simulation of TD-BNP

Boxes were constructed using Gromacs 2023.3 software, One BSA molecule and ten Tidesglusib molecules were randomly distributed into the box. Subsequently, water molecules were added to solubilise the system, and Na^+ and Cl^- ions were added to neutralise the net charge within the system.

All kinetic simulations were carried out using Gromacs version 2023.3, and 100 ns kinetic simulations were performed after energy minimisation and pre-equilibration with NPT tether. Simulation parameter settings: energy minimisation (1000 kJ/mol/nm) was performed using the steepest descent method Steep, followed by 500 ps of NVT and NPT pre-equilibrium simulations. The temperature was set to 298 K. A V-rescale thermostat was used for temperature coupling, and a C-rescale pressure controller was used for pressure-temperature coupling, with the pressure set to 1 bar. Long-range van der Waals interactions were truncated at 10 Å. A particle-mesh Ewald was used to handle electrostatic interactions. The production simulation step size was 2 fs, and trajectories were saved every 10 ps. VMD obtained snapshots of the trajectories.

2.6. Preparation and characterization of TD-BNP@DBBM

In the six-well plate, 20 mg of DBBM was added to each well, and 1 mL of 20 μg/mL of TD-BNP was added, lyophilized and prepared for use. The morphology of TD-BNP@DBBM could be observed by SEM, the difference of functional groups between DBBM and TD-BNP@DBBM was observed by FT-IR, and the release rate of TD-BNP from TD-BNP@DBBM was detected by UV spectrophotometer.

2.6.1. In vitro cell culture

MC3T3-E1 cells were incubated in an Alpha complete Medium. After 48 h, MC3T3-E1 cells were passaged when they reached 80–90 % confluence, and the subsequent experiments were conducted using cells that had undergone up to three passages.

RAW264.7 cells were incubated in an Dulbecco's Modified Eagle Medium. After 48 h, RAW264.7 cells were passaged when they reached 80–90 % confluence, and the subsequent experiments were conducted using cells that had undergone up to three passages.

2.6.2. Cell viability

The MC3T3-E1 cells' viability was evaluated using a live/dead staining kit. Cells were added to 12-well plates and then cultured for 1, 2, and 3 days. The density of cells was 1×10^5 in each well. After being immersed in the live/dead kit for 30 min, cells were captured using a fluorescence microscope (Olympus, Japan).

MC3T3-E1 cells were added to 96-well plates at a 2×10^3 density per well for 1, 2, and 3 days to assess cell proliferation. At a particular point, a 100 μL new medium with 10 μL of CCK8 reagent was introduced. Following 2 h of co-culture, absorbance was measured at 450 nm using a microplate reader.

2.6.3. Hemolysis rate

Fresh blood was collected from rats and centrifuged at 3000 rpm for 15 min. Then, 1 mL of different concentrations of TD-BNP (0–160 μg/mL), as well as 1 mL ultrapure water and PBS, were used as the control group. These were mixed with 20 μL of hematocrits, respectively, and co-incubated for 4 h at 37 °C. The supernatant was then centrifuged to obtain the supernatant, and a microplate reader measured the absorbance value at 542 nm.

2.6.4. Cell adhesion

MC3T3-E1 cells were added into 12-well plates at a density of 1×10^5 cells per well and then cultured for 8 h. After fixing the cells for 30 min with 4 % paraformaldehyde, they were stained with rhodamine-phalloidin for 30 min to observe the cell adhesion and DAPI for 3 min to see the nucleus.

2.6.5. Cell migration

Cell migration was assessed using the Transwell Migration Assay. Following a 24-h co-cultivation period in α-Minimum Essential Medium,

Table 1
Primer sequences of target genes.

Gene		Primer sequences(5′-3′)
RUNX2	F	CCGAAATGCCTCCGCTGTTATG
	R	TCTGTCTGTGCCTTCTTGGTTCC
OSX	F	AGTTCACCTGCCTGCTCTGTTC
	R	GCGGCTGATTGGCTTCTTCTTC
OCN	F	CAAGCAGGAGGGCAATAAGGTAGTG
	R	CATACTGGTCTGATAGCTCGTCACAAG
Wnt3a	F	TCTGGTGGTCCTTGGCTGTG
	R	GCTGTTGCTGACGGTGGTG
β-catenin	F	GCTGACCAAACTGCTAAATGACGA
	R	TGTAGGGTCCCAGCGGTACAA
GSK3β	F	AACTACCAAATGGGCGAGACACAC
	R	GCGTTGGCAGGCGGTGAAG
INOS	F	GGGGAGCCATTTTGGTGACT
	R	AAGGTAGTCAGTCCCTGGCTTATGG
Arg-1	F	AGACAGCAGAGGAGGTGAAGAGTAC
	R	AAGGTAGTCAGTCCCTGGCTTATGG
GAPDH	F	GCTCTCCAGAACATCATCC
	R	TGCTTCACCACCTTCTTG

MC3T3-E1 cells underwent a 30-min fixation with 4 % paraformaldehyde and a 15-min staining process with crystal violet, cotton was used to remove the non-migratory cells. Migratory cells at the base of the filter were visible under a microscope (Olympus, Japan).

2.6.6. Osteoblast differentiation assay

10 mg of each group of material was added to the 12-well plate, and MC3T3-E1 cells were spread in the 12-well plate at a density of 1×10^5 each well, and the fluid change was performed every two days. On day 5, PBS solution washed away the material in the alkaline phosphatase-stained well plates, alkaline phosphatase was measured on day 7, and when ARS was measured, PBS solution was washed away from each group of material on day 12 followed by incubation for two days and then removing the wells from the plate. Direct co-culture of DBBM and TD-BNP@DBBM with cells in well plates. Cells were visualized under a microscope (Olympus, Japan).

2.6.7. Western Blotting

20 mg of each group of material was added to the 6-well plate, and MC3T3-E1 cells were spread in the 6-well plate at a density of 2×10^5 each well, DBBM and TD-BNP@DBBM were maintained in an α-Minimum Essential Medium for 14 days to cultivate MC3T3-E1 cells. The proteins were extracted using RIPA buffer, and their concentrations were tested using the BCA Protein Assay Kit. Following their separation using 10 % SDS-PAGE, the measured proteins were transferred to membranes. After blocking, primary antibodies were incubated on the membranes for an overnight period at 4 °C. Subsequently, secondary antibodies were applied to the membranes. Enhanced chemiluminescence reagent was used to identify proteins.

2.6.8. RNA extraction and analysis

20 mg of each group of material was added to the 6-well plate, and MC3T3-E1 cells were spread in the 6-well plate at a density of 2×10^5 each well, DBBM and TD-BNP@DBBM were maintained in an α-Minimum Essential Medium for 14 days to cultivate MC3T3-E1 cells. Using the Trizol reagent, the total RNA was extracted. Next, cDNA synthesis was done using a cDNA kit from the same vendor. RT-PCR was carried out using a SYBR Green Master Supermix kit. The reference gene was GAPDH, Using the $2^{-\Delta\Delta Ct}$ approach to determine the gene levels. Primer sequences are displayed in Table 1.

2.6.9. Immunofluorescence staining

MC3T3-E1 cells were spread in the 12-well plate at a density of 1×10^5 each well, 10 mg DBBM and TD-BNP@DBBM were maintained in Essential Medium for 3 days to cultivate cells. The cells were fixed using 4 % paraformaldehyde after being cultured. The cells were then made permeable for 10 min with Triton X-100. After being blocked for 30 min, the cells were treated with primary antibodies and incubated at 4 °C overnight. Afterwards, they were treated with a secondary antibody related to phalloidin. Ultimately, DAPI was used to colour the nucleus, and pictures were taken with a fluorescence microscope (Olympus, Japan).

Table 2
Databases of network pharmacology.

Name	web address
DrugBank	https://go.drugbank.com/
Swiss	http://swisstargetprediction.ch/index.php
GeneCards	https://www.genecards.org/
OMIM	https://www.omim.org/
Venny ver.2.1	https://bioinfogp.cnb.csic.es/tools/venny/
STRING	https://cn.string-db.org/
UniProt	https://www.uniprot.org/
DAVID	https://david.ncifcrf.gov/tools.jsp
PDB	https://www.rcsb.org/
PubChem	https://pubchem.ncbi.nlm.nih.gov/

2.6.10. Network pharmacology

From the DrugBank database and the Swiss Target Prediction database to find possible target genes for Tideglusib. The word osteogenic was entered into the OMIM and GeneCards databases, respectively, to identify all potential target genes. The top 2000 target genes were screened. All identified target genes were normalised and submitted to the UniProt database to obtain their UniProt IDs. Target genes with duplicate Unitprot IDs were deleted. A Venn diagram was generated using the online tool Venny ver. Version 2.1 to illustrate the cross-targeting of Tideglusib and osteogenesis-related genes. The overlapping targets and active compounds were imported into Cytoscape version 3.7 for network construction. The common targets were processed using STRING before being imported into the DAVID database database to investigate KEGG and GO pathways. The PDB database was used to get the protein structures, while the chemical structures were obtained from the PubChem database. AutoDockTools 1.5.6 was used to process protein, web addresses are displayed in Table 2.

2.6.11. In vivo bone defect model and materials implantation

Sprague-Dawley (SD) rats (male, n = 18, average weight approximately 250 g) were acquired from Nanjing Medical University's Animal Experiment Center and kept separately in cages. Ethical approval (Ethics No. 2312029) was obtained from the Ethics and Animal Research Committee of Nanjing Medical University, adhering to IACUC guidelines. Under pentobarbital sodium anesthesia (20 mg/kg), using a high-speed skull drill, bilateral full-thickness bone defects (5 mm diameter) [33,34] were made after anesthesia. The rats were divided into 3 groups: control, DBBM, and TD-BNP@DBBM insertion group. While the control group received no treatment, the defects in the DBBM and TD-BNP@DBBM groups were filled with these materials. Closure of the dura mater and scalp in layers was performed with absorbable sutures (Fig. S2).

2.6.12. Micro-CT analysis

Rat calvarial bones were collected at 4 and 8 weeks after DBBM and TD-BNP@DBBM were implanted. After trimming the rat's cranium and removing the periosteum, the DBBM that hadn't undergone osseointegration were shed off along with the periosteum. The samples were fixed for 48 h in 4 % paraformaldehyde. They were then rinsed overnight with running water and then stored in 70 % anhydrous ethanol solution for subsequent radiological and histological evaluation. To assess the new bone development, samples were scanned by micro-CT equipment (Skysacn, Kontich, Belgium) and analysed using Skyscan CTAn software. Around the defect location, the regions of interest were established. After evaluating the morphology of the bones, parameters were

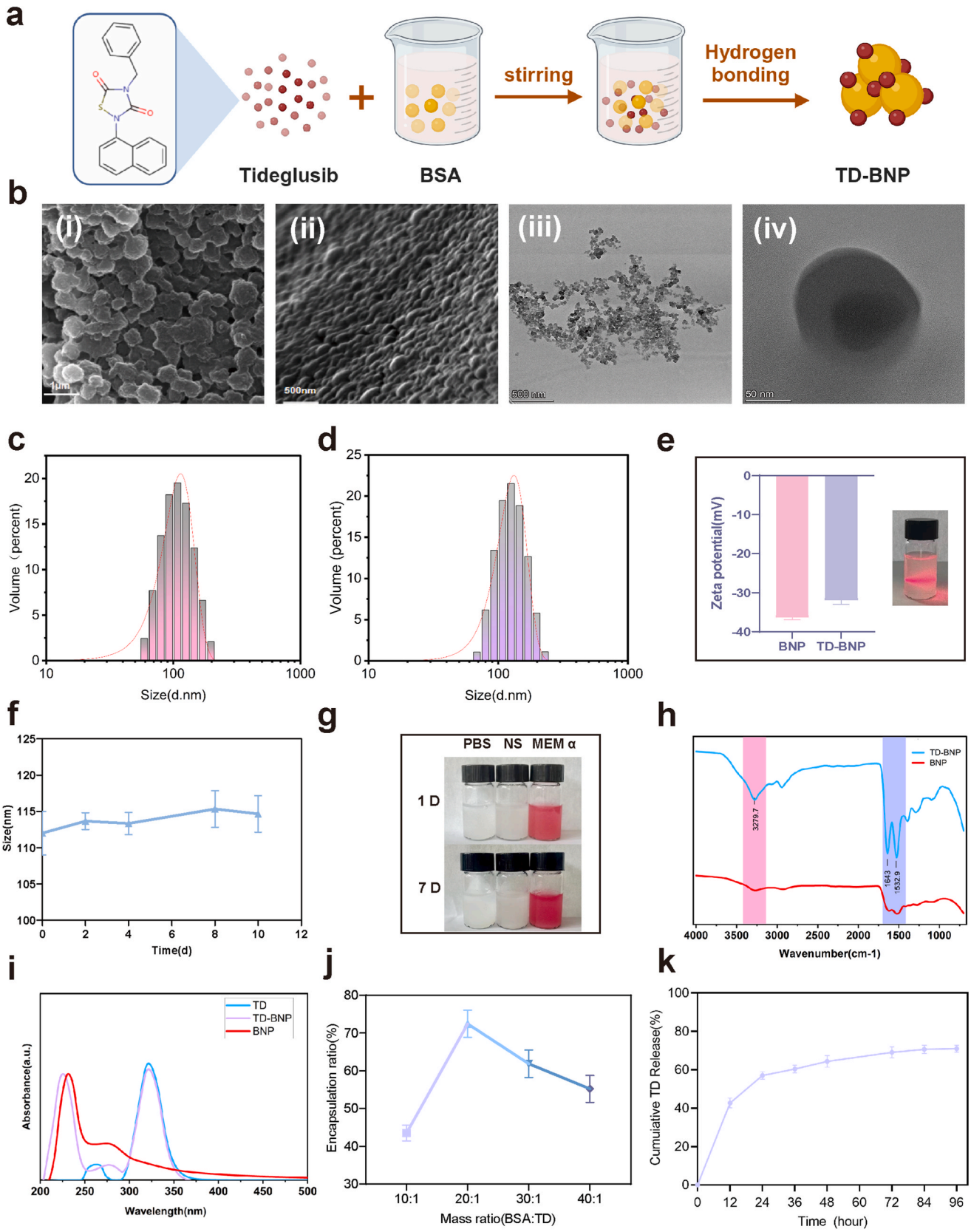

Fig. 2. Characterisation of TD-BNP. (a) Schematic representation of BNP (TD-BNP: tideglusib binds to BSA nanoparticles via hydrogen bonding). (b) Representative pictures of SEM (i, ii). Representative images of TEM (iii,iiii). (c,d) The hydration size distribution of BNP and TD-BNP by DLS. (e) Zeta potential of BNP and TD-BNP. (f) Hydrodynamic sizes of TD-BNP during storage measured by DLS. (g) Dispersibility and stability of TD-BNP in PBS, 0.9 % NaCl, and Alpha-MEM on days 1 and 7. (h) FT-IR analysis of functional groups in BNP and TD-BNP. (i) UV–vis absorption spectra of TD, BNP, and TD-BNP. (j) Encapsulation rate of TD at different mass ratios (BSA: TD). (k) The cumulative release of TD from TD-BNP in PBS.

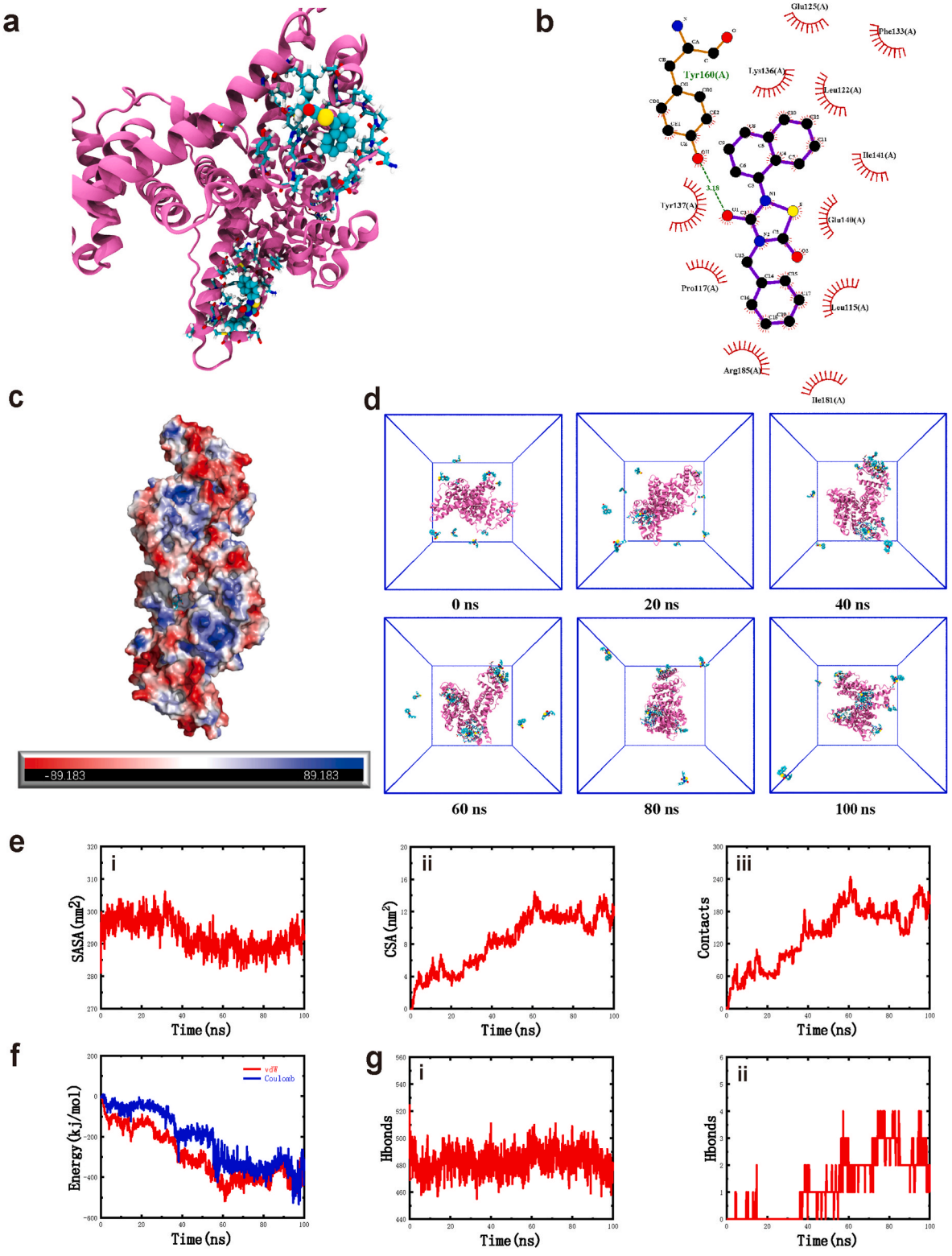

Fig. 3. Molecular docking and molecular dynamics simulations of TD and BSA. (a) Three-dimensional structure of TD-BNP molecular docking. (b) Two-dimensional structure of TD-BNP. (c) Surface electrostatic forces of TD-BNP. (d) Representative snapshots of the self-assembly process of BSA with Tideglusib molecules during 100 ns kinetics. (e) 100 ns kinetics of (i) the solvent accessible surface area (SASA) of BSA, (ii) the contact surface area (CSA) between BSA and Tideglusib molecules, and (iii) the number of atomic contacts between BSA and Tideglusib molecules. (f) Van der Waals (vdW) as well as Coulomb interactions (Coulomb) between Tideglusib and BSA during 100 ns kinetics. (g) 100 ns kinetics of (i) changes in the number of hydrogen bonds in BSA's own memory. (ii) changes in the number of hydrogen bonds between Tideglusib and BSA.

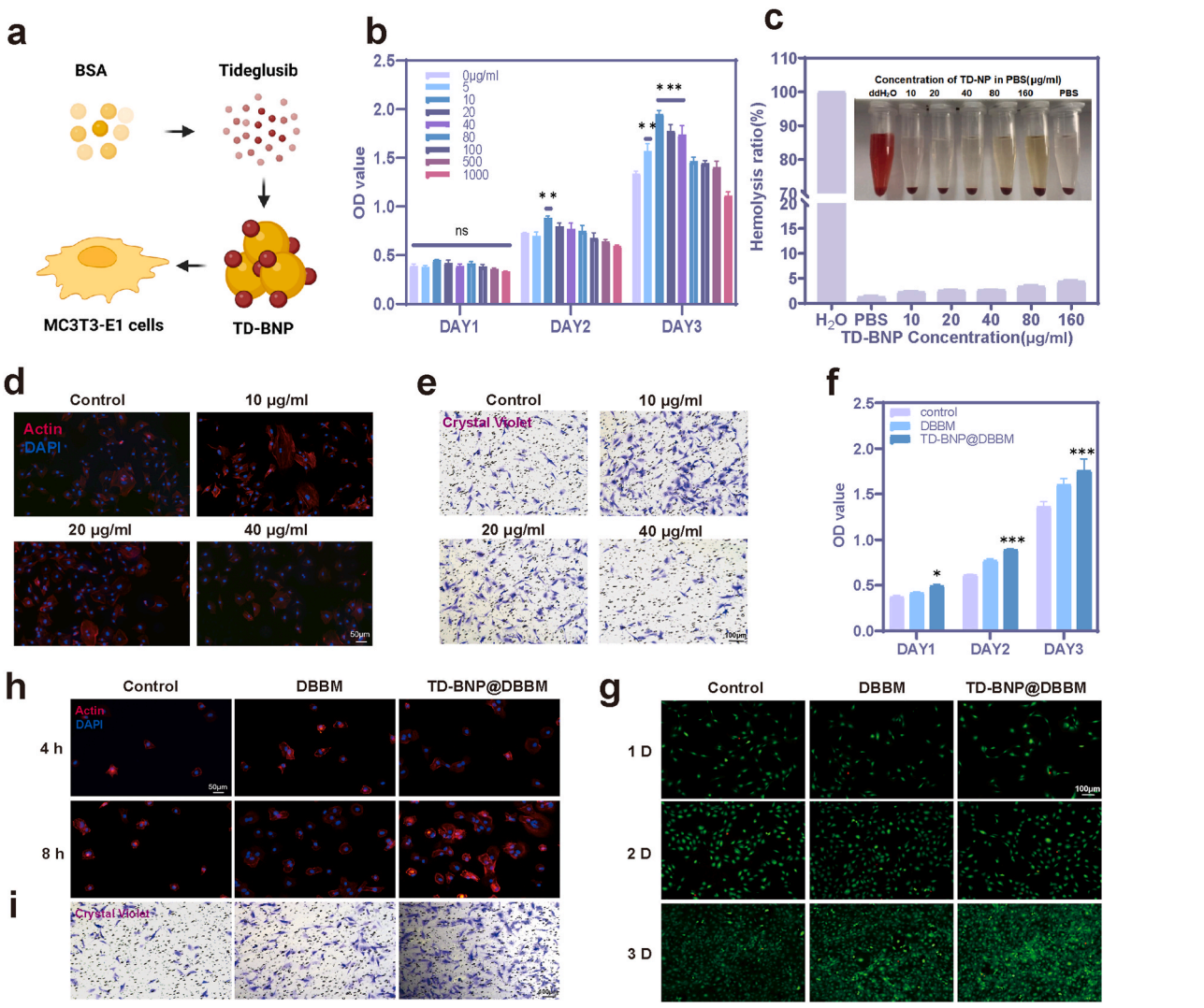

Fig. 4. Biocompatibility of TD-BNP and TD-BNP@DBBM. (a) Schematic diagram of TD-BNP preparation process and co-culture with cells.(TD-BNP: Tideglusib-loaded bovine serum albumin nanoparticles were taken up by cells.) (b) Cell proliferation in different concentrations of TD-BNP solution was assessed by CCK8 assay at different points in time. (c) Hemolysis rate of TD extracts and their quantitative results. (d) Fluorescence images of cell adhesion after incubating cells with various concentrations of TD-BNP. (e) Transwell migration assay results of MC3T3-E1 with various doses of TD-BNP. (f) Proliferation of MC3T3-E1 cells on DBBM, TD-BNP@DBBM assessed by CCK8 assay after culturing at different points in time. (g) Cells adhesion on the DBBM and TD-BNP@DBBM after Live/Dead staining. (h) Fluorescence images of cells cultured with DBBM and TD-BNP@DBBM for 4 h and 8 h. (i) Transwell migration assay results of different treatments. Cells were co-cultured with DBBM and TD-BNP@DBBM.

computed, including the bone volume fraction (BV/TV, %), trabecular thickness (Tb. Th, μm), trabecular number (Tb. N, 1/mm) and bone mineral density (BMD, g/cm^3).

2.6.13. Histological and immunohistochemical analysis

After completion of decalcification at room temperature, bone tissues were dehydrated, dipped in wax, and paraffin-embedded in an Advanced Intelligent Processor (Leica, Germany) and Tissue Embedding Station (Leica, Germany). Bone tissues were sectioned in the coronal direction using a microtome (Leica, Germany). Sections 4 μm thick were taken from the paraffin blocks and centred on the defect area, and the sections were stained with H&E, Masson trichrome staining, immunofluorescence staining, and immunohistochemical staining.

2.7. Statistical analysis

Statistical analysis was performed using GraphPad Prism 9.5 software. The data were presented as mean ± standard deviation. The normality of the data was checked by Shapiro-Wilk test and Levene's test was used to assess the homogeneity of variance. The analysis of variance (ANOVA) with Tukey's post hoc test was conducted for comparisons. Ns, not significant, *$p < 0.05$, **$p < 0.01$, and ***$p < 0.001$.

3. Results and discussion

3.1. Characterization of TD-BNP and TD-BNP@DBBM

TD-BNP was synthesised by selecting a natural small molecule compound, TD, which was encapsulated by BSA nanoparticles and administered to achieve a slow-release and long-lasting therapeutic effect of TD exact site in vivo. TD-BNP suspension appeared milky white (Fig. S1).

The physicochemical properties of nanomaterials, such as structural composition, size, and particle size stability, have an important influence on the biological response of cells. SEM and TEM (Fig. 2b) representative pictures showed that TD-BNP has a spherical shape. The hydration size distribution of BNP by DLS was about 100 nm (Fig. 2c), and the hydration size distribution of TD-BNP was about 110 nm

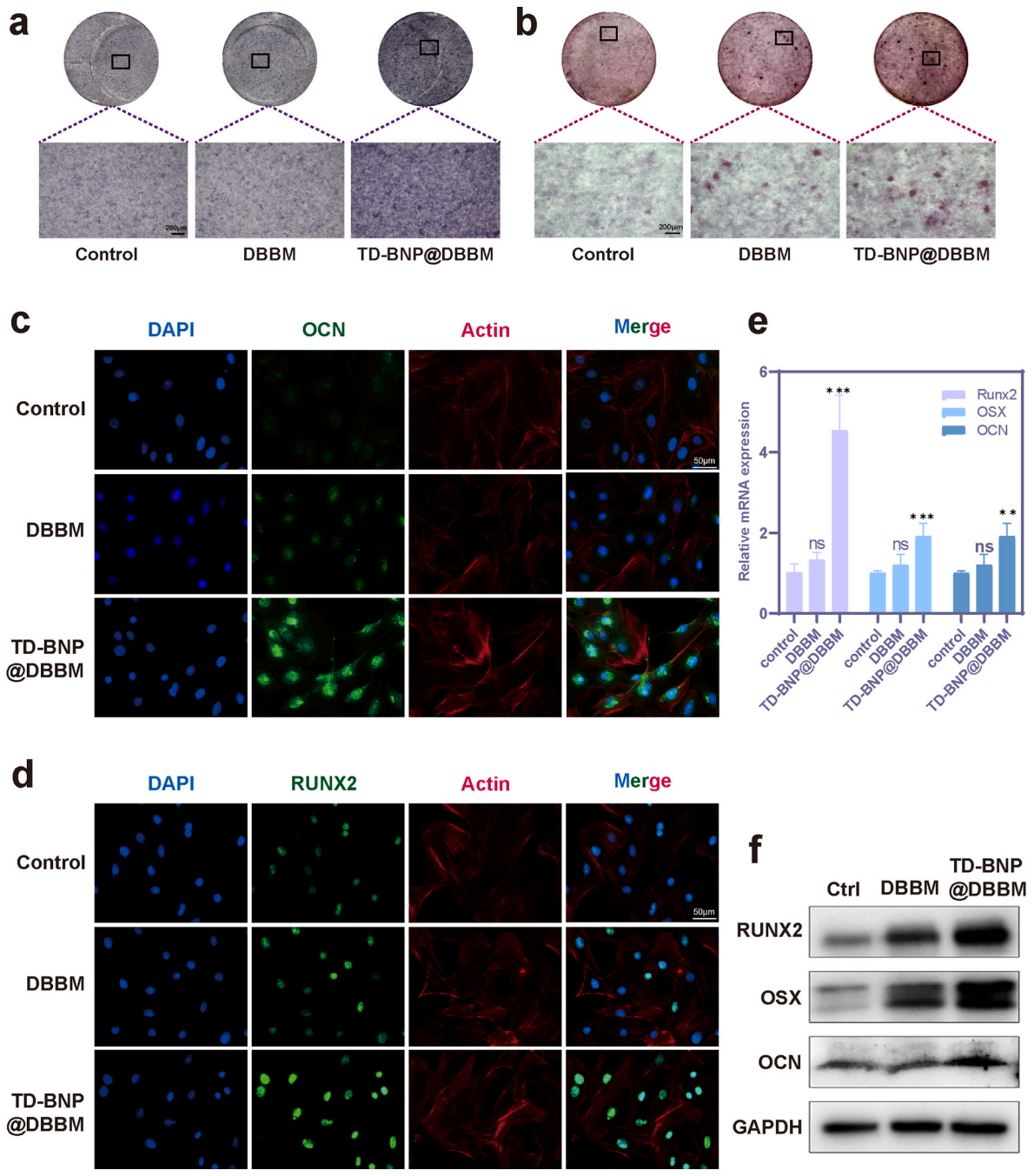

Fig. 5. TD-BNP@DBBM promoted osteogenic differentiation. (a) The ALP was staining on three groups (control, DBBM, and TD-BNP@DBBM) for 7 days. (b) ARS were stained after 14 days of culture. (c,d) Using immunofluorescence staining, the expression levels of RUNX2 and OCN were assessed. (e) RT-qPCR analysed Runx2, OCN, and OSX expression levels after 14 days. (f) Runx2, OSX, and OCN protein expression after a 14-day culture on three groups (control, DBBM, and TD-BNP@DBBM).

(Fig. 2d). The zeta potential indicated a homogeneous and stable nanoparticle size after drug loading (Fig. 2e).

The hydrodynamic size of TD-BNP was measured by DLS during storage, and no significant change in particle size was observed (Fig. 2f). TD-BNP was stored in different solutions, and there was no significant change in the dispersion and stability of TD-BNP in PBS, 0.9 % NaCl, or Alpha-MEM on days 1 and 7 (Fig. 2g). FT-IR showed that the waveforms of the TD-BNP and BSA nanoparticles were different and revealed changes in the characteristic peak at~3279 cm^{-1}, which suggests that TD and BSA were bonded together by hydrogen bonding, indicating that TD had been successfully loaded into the nanoparticles (Fig. 2h). UV–Vis absorption spectra revealed that TD-BNP showed characteristic peaks of TD and BSA (Fig. 2i). The best TD encapsulation rate was about 72.4 % when the mass ratio of BSA to tideglusib was 20:1. In order to further investigate the reason, the morphology of TD-BNP with different mass ratios was observed by transmission electron microscopy(Fig. S3a), and TD-BNP was of spherical shape when the mass ratios were 10:1 and 20:1, and the particle size increased slightly with the increase of mass ratio, and the particle size also significantly increased when the mass ratios were increased to 30:1 and 40:1. When the mass ratio was increased to 30:1 and 40:1, TD-BNP lost its original shape and became disordered, and the particle size also increased significantly. The hydrated particle size and zeta potential results(Figs. S3b and c) showed that the hydrated particle size increased significantly when the mass ratio reached 30:1,

and the zeta potential results showed that the nanoparticle stability decreased significantly when the mass ratio reached 30:1. And the release experiments showed that TD was successfully released, at a rate of 69.1 % at 96 h (Fig. 2j and k).

Molecular docking simulation experiments showed that TD binds to the active site of BSA, obtaining the lowest binding energy arrangement and the best 3D molecular docking structure (Fig. 3a), in which TD can bind to BSA in the molecular pocket through hydrogen bonding and the formation of forces represented by electrostatic potential energy and van der Waals forces. Hydrogen bonding and these forces can enable the two to form a tight and stable complex (Fig. 3b and c).

The interaction of BSA with TD was visualized using MD simulations, and the stability of the self-assembled nanostructures was assessed. Tideglusib molecules were continuously brought into contact with BSA during the kinetic process and were gradually and stably adsorbed onto BSA. At the end of the 100 ns kinetic simulation, a total of 6 out of 10 Tideglusib molecules were stably adsorbed on the BSA (Fig. 3d).

Fig. 3e analysed the changes in the solvent-accessible surface area (SASA) of BSA, the contact surface area (CSA) between BSA and Tideglusib molecules, and the number of atomic contacts during the kinetic process. The SASA of BSA gradually decreased as Tideglusib molecules adsorb on BSA (Fig. 3e–i), which was caused by the fact that the portion of residues originally in contact with the solvent became in contact with the Tideglusib molecule. With the adsorption of Tideglusib molecules on BSA, the contact surface area and the number of atomic contacts between Tideglusib and BSA increased (Fig. 3e, ii, iii), which was consistent with the trend of (Fig. 3e–i), showing a gradual decrease in the SASA of BSA.

The changes in van der Waals (vdW), as well as Coulomb interactions (Coulomb) between Tideglusib and BSA during self-assembly, were

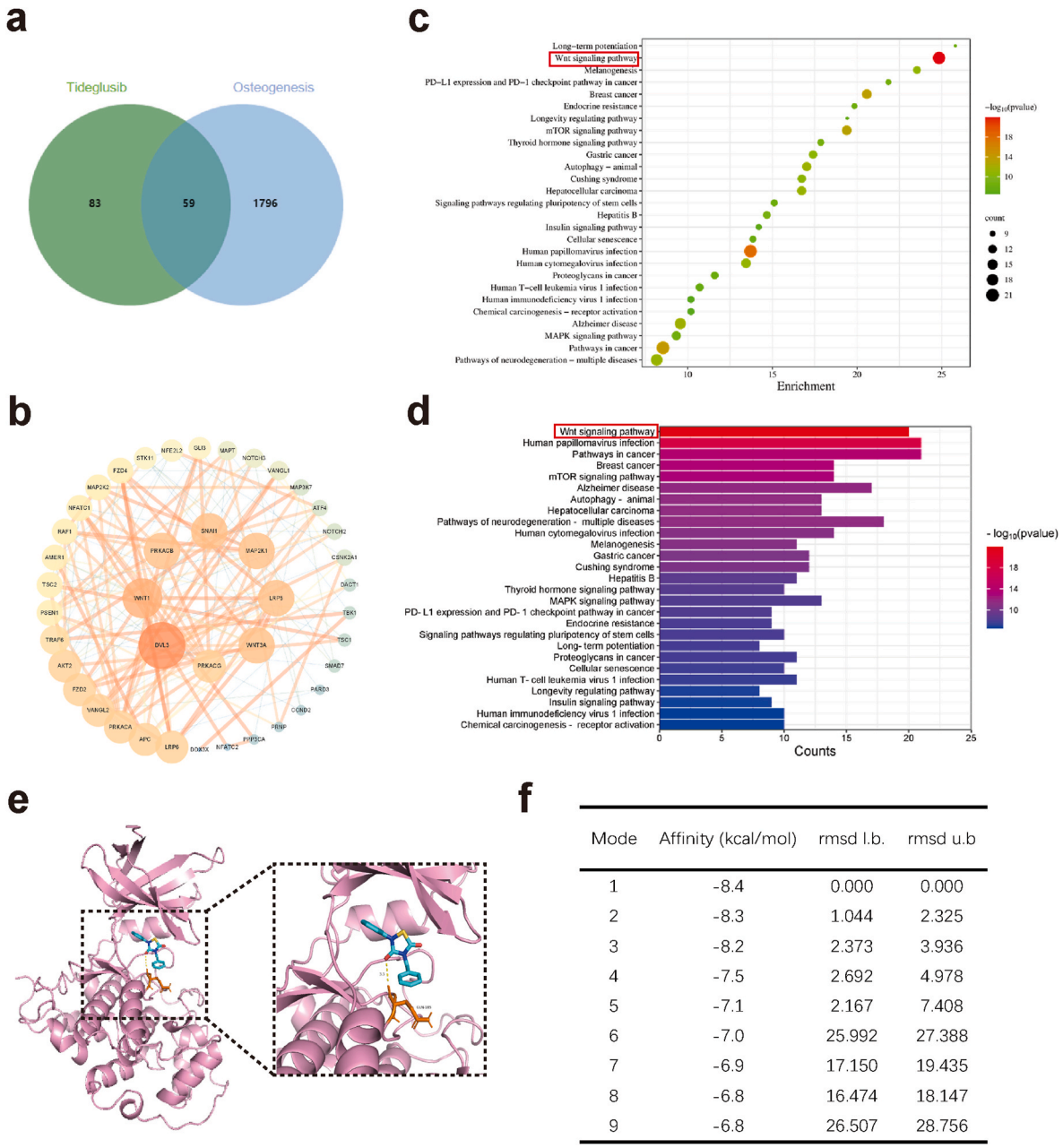

Mode	Affinity (kcal/mol)	rmsd l.b.	rmsd u.b
1	-8.4	0.000	0.000
2	-8.3	1.044	2.325
3	-8.2	2.373	3.936
4	-7.5	2.692	4.978
5	-7.1	2.167	7.408
6	-7.0	25.992	27.388
7	-6.9	17.150	19.435
8	-6.8	16.474	18.147
9	-6.8	26.507	28.756

Fig. 6. Screening target genes and pathways through network pharmacology and molecular docking. (a) Venny map of intersection target genes between tideglusib and osteogenesis. (b) The protein-protein interaction network between tideglusib and osteogenesis target. (c,d) GO and KEGG enrichment analysis of tideglusib and osteogenesis. (e,f) Molecular docking. Representative images of tideglusib active ingredients combined with GSK-3β and binding energy.

shown in Fig. 3f. The adsorption of Tideglusib molecules on BSA was a joint result of van der Waals interactions as well as electrostatic interactions. The Tideglusib molecules first come into contact with some amino acid residues of BSA, and the van der Waals interactions generated by the contact between the two molecules gradually caused the Tideglusib molecules to adsorb onto the BSA. As the degree of adsorption deepens, the electrostatic interaction between Tideglusib molecules and BSA was also gradually enhanced, which enabled Tideglusib molecules to be stably adsorbed on BSA (Fig. 3f), As can be seen from (Fig. 3g–i), the number of hydrogen bonds within the BSA decreases with the slight loosening of its own structure at the initial time, but it is gradually regionally stabilized during the subsequent simulations. And from (Fig. 3g–ii), it can be seen that with the adsorption of Tideglusib molecules on BSA, hydrogen bonds are also formed between Tideglusib molecules and BSA, resulting in hydrogen bonding interactions.

TD-BNP@DBBM was obtained by combining 10 μg/mL TD-BNP with DBBM (Fig. S4a), IR spectroscopy results showed that the characteristic peak of BNP appeared near 1600 cm^{-1} for TD-BNP@DBBM compared with DBBM, and the wave peak at 3279 cm^{-1} was changed, which indicated that TD-BNP successfully modified DBBM (Fig. S4b); TD-BNP was released faster in the first 18 h, and the release gradually leveled off after 18 h (Fig. S4c).

3.2. Biocompatibility in vitro

To investigate the biocompatibility of TD-BNP and test the cytotoxicity of MC3T3-E1 cells, CCK-8 assay was used, which suggested high cell viability even at high concentrations after co-incubation of TD-BNP for 1, 2 and 3 days, with the higher cell viability at 10, 20, and 40 μg/mL, among which 10 μg/mL was the best (Fig. 4b). Then, in vivo, the biological toxicity of tideglusib was further examined by hemolysis assay, which showed that no hemolysis occurred even at high concentrations of TD-BNP (Fig. 4c). It was further verified by cell adhesion assay and cell migration assay that TD-BNP at 10 μg/mL was the most effective for cell adhesion and migration (Fig. 4d and e). Subsequently, the optimal cytocompatibility was the TD-BNP@DBBM group, which was demonstrated by cck-8 and cell live-dead staining experiments on MC3T3-E1 cells, cck-8 experiments demonstrated better cell proliferation in the TD-BNP@DBBM group, and live-dead staining experiments proved that there was no significant toxicity in all groups, and there were more live cells in the TD-BNP@DBBM group (Fig. 4f and g). The bioactive capacity of each group was further tested by cell adhesion assay and cell migration assay, as well as superior cell adhesion and migration in the TD-BNP@DBBM group (Fig. 4h and i).

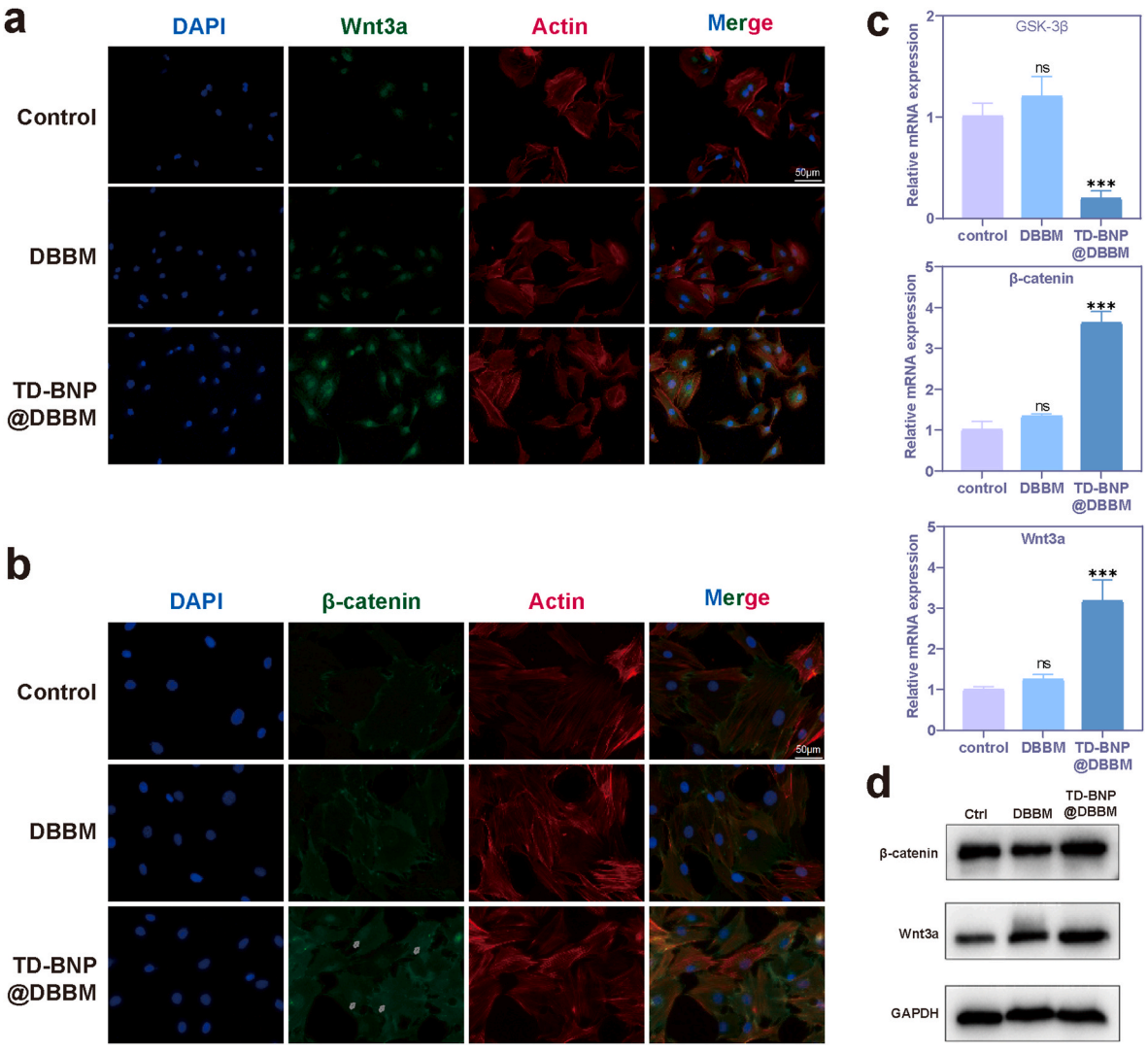

Fig. 7. Validating the Purposeful Pathway for Network Pharmacology Screening. (a,b) Using immunofluorescence staining to examine the expression of wnt3a and β-catenin. (c) PCR analysed the levels of wnt3a, β-catenin, and GSK-3β after 14 days. (d) The protein levels of wnt3a and β-catenin after culturing on three groups (control, DBBM, and TD-BNP@DBBM) for 14 days.

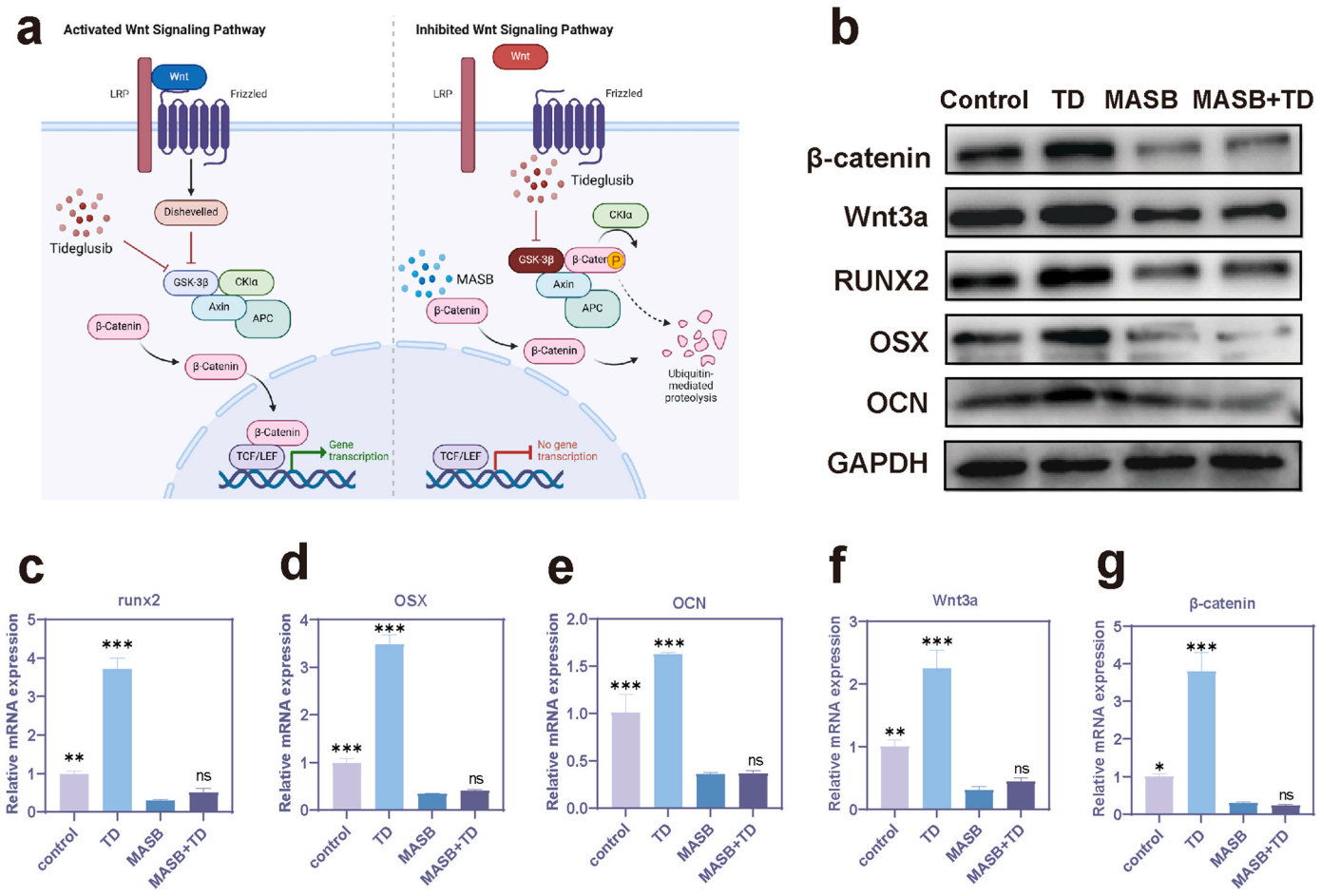

Fig. 8. Further validation can be achieved by adding a pathway inhibitor. (a) Schematic diagram of activation and inhibition of target pathways. (b)The protein levels of wnt3a, β-catenin, Runx2, OSX, and OCN were examined by western blot after culturing on four groups (control, TD, MASB, TD + MASB) for 14 days. (c–g) The levels of wnt3a, β-catenin, Runx2, OSX, and OCN were analysed by RT-qPCR after culturing on four groups (control, TD, MASB, TD + MASB) for 14 days.

3.3. TD-BNP@DBBM promoted the osteogenic differentiation

The primary objective of this study was to enhance the osteoinductivy of DBBM by surface-modifying it with nanoparticles that exhibit sustained-release capabilities of TD. However, TD-BNP lacks supporting effect and cannot be used alone in animal models or clinical applications. Consequently, we did not include pure TD-BNP as a control group in our experiments. Cells were cultivated with DBBM and TD-BNP@DBBM and stimulated toward osteogenic differentiation. After 7 days of osteogenic induction, the expression of ALP (the recognised norm of early osteogenic differentiation) was higher in the TD-BNP@DBBM group, and staining with ARS after osteogenic induction for 14 days showed an increase in calcium deposition in the TD-BNP@DBBM group compared to other groups (Fig. 5a and b).

Given the limited research on the mechanisms underlying bone repair involving TD-BNP@DBBM, the potential molecular mechanism of TD-BNP@DBBM in promoting bone repair was explored by examining osteogenesis-related gene and protein expression. RUNX2 is a pivotal transcription factor unique to osteogenesis and is considered to be an early indicator of the osteogenic differentiation process [35,36]. OSX is considered a marker associated with osteogenic mineralisation, while OCN is considered a marker of late osteogenic differentiation [37–39]. RUNX2 and OCN fluorescence expression was detected by cellular immunofluorescence, and the fluorescence expression results showed that it was increased in the TD-BNP@DBBM group (Fig. 5c and d), the expression of mRNA and protein of osteogenic indicators was detected by qRT-PCR and Western blotting (Fig. 5e and f). RUNX2, OSX, and OCN expression were significantly higher in the TD-BNP@DBBM group. In the DBBM group, RUNX2, OSX, and OCN expression was higher than in the control group, but not statistically different. To further explore the reasons for the elevated expression of osteogenic indicators, expression of osteogenic indicators in the control, BNP, TD, and TD-BNP group was detected by qRT-PCR, Western Blotting and immunofluorescence. As shown in the results of Figs. S5a–d, TD promoted an increase in the expression of osteogenesis-related genes and proteins, whereas BNP was not significantly different from the control group and did not promote osteogenic differentiation, suggesting that BNP only served as a carrier and did not induce osteogenic activity.

3.4. TD-BNP@DBBM enhanced the osteogenesis by activating the wnt/β-catenin pathway

TD, as a small molecule thiadiazolidinone drug, was first used in clinical studies of Alzheimer's disease, which can improve learning and memory and induce neuronal regeneration [40–42]. It can improve the proliferation of epidermal stem cells in rats, which can contribute to the repair of defective wounds [43] and promote the formation of reparative dentin at the perforations of the dental pulp of SD rats [23]. However, there are no studies on the mechanisms of TD on the proliferation and osteogenic differentiation of MC3T3-E1 cells. To further investigate the mechanism of Tideglusib in promoting osteogenic differentiation, this study further screened the core targets of TIdeglusib and osteogenesis-related genes by network pharmacology, and the mechanism was targeted to the Wnt/β-catenin pathway.

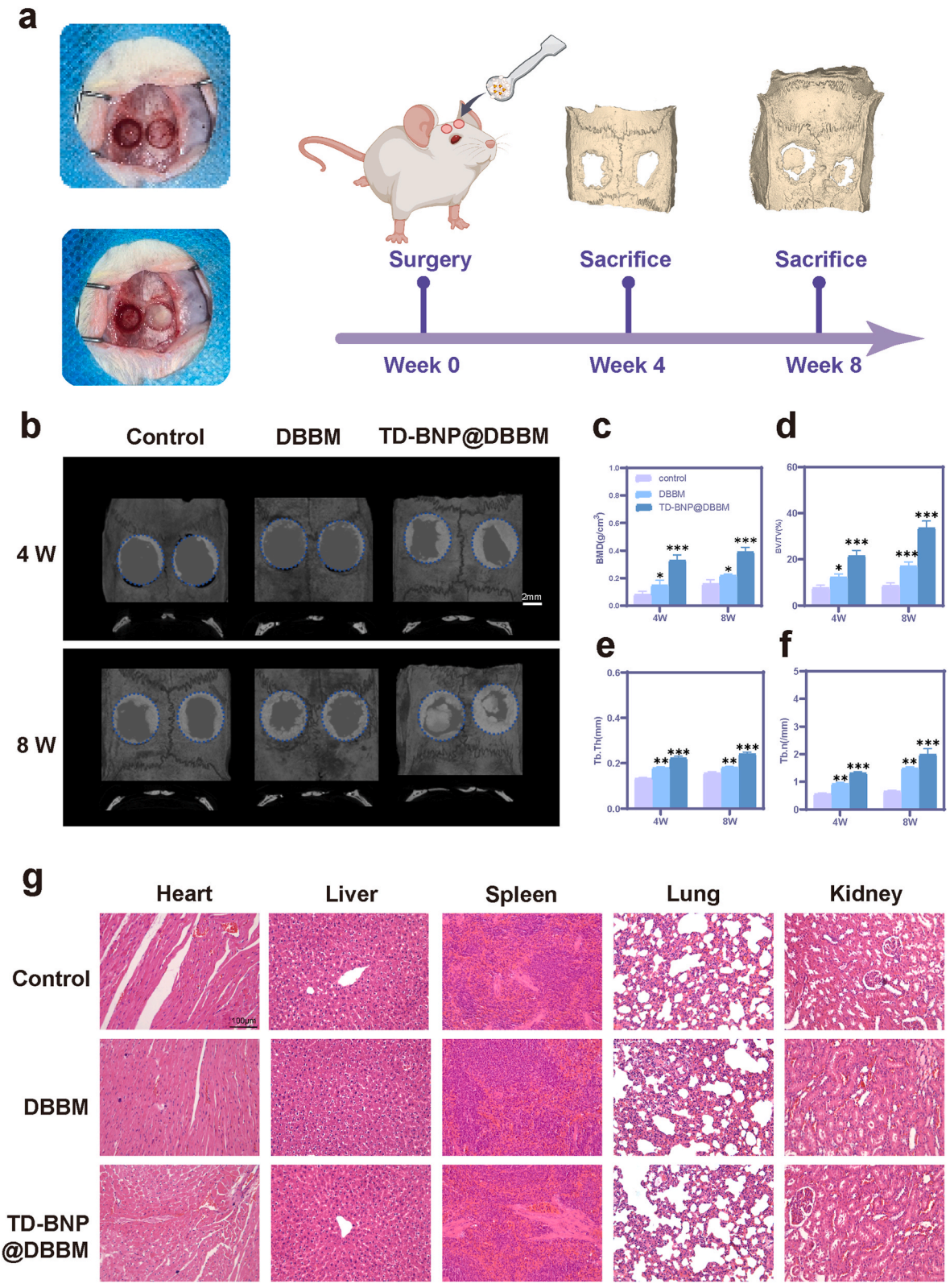

Fig. 9. TD-BNP@DBBM enhanced bone repair in critical-sized calvarial lesions. (a) Diagram illustrating the experimental design used to evaluate the osteogenic potential of TD-BNP@DBBM. (b) Representative 3D-reconstructed images of the skulls from each experimental group. (c–f) Quantitative assessments of the bone microstructural parameter. (g) H&E staining of the heart, liver, spleen, lungs, and kidneys of 8 W rats.

The intersecting targets of TD with osteogenesis were screened by Drugbank and Genecard (Fig. 6a and b). In the GO and KEGG enrichment analysis (Fig. 6c and d), it was discovered that TD modulated the Wnt/β-catenin pathway to control the osteogenic development of MC3T3-E1 cells.

Molecular docking of Tideglusib to GSK-3β, a target protein of this pathway, was performed. The molecular docking results of TD and protein GSK-3β (Fig. 6e and f) show that the fit of the protein to the small

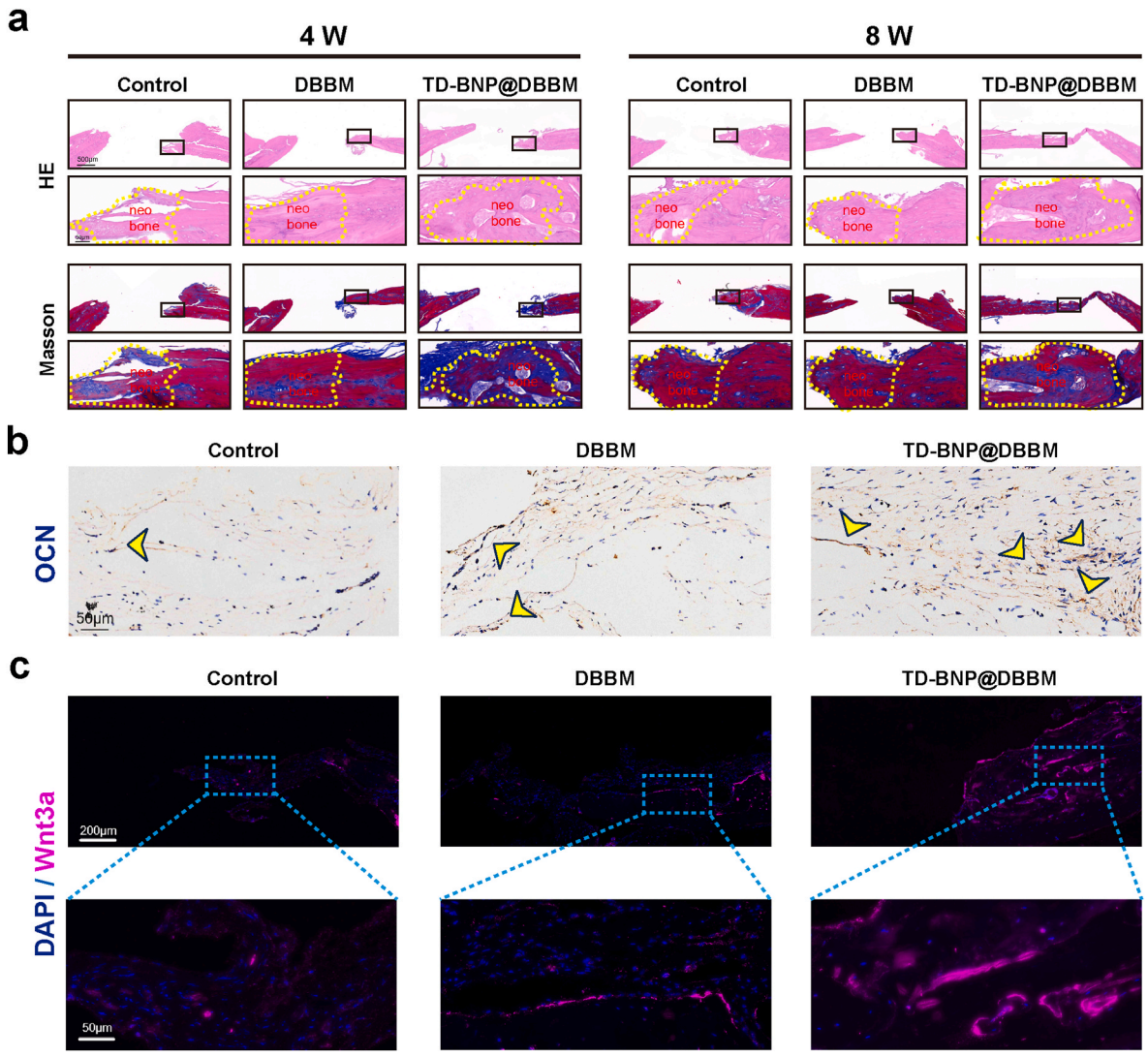

Fig. 10. Histological staining. (a) H&E and Masson's staining of the tissues at 4 and 8 weeks. (b) The immunohistochemical expression of OCN. (c) Immunofluorescent staining for Wnt3a.

molecule receptor binding pocket is high, and the nine docking results with the lowest molecular binding energies were all lower than −6.5 kcal/mol, which could bind under natural conditions. The small molecule drug TD formed a hydrogen bond with the protein GSK-3β. To elucidate its mechanisms, we examined the impact of TD-BNP on the target pathway of MC3T3-E1 cells.

The Wnt/β-catenin signalling pathway stimulates the proliferation of pre-osteoblasts, which in turn induces osteoblast formation and differentiation [44,45]. The classical Wnt signalling pathway is mediated by β-catenin [32,46–48], and in the absence of Wnt protein stimulation or when the GSK-3β protein in the cytoplasm is abnormally activated, intracytoplasmic β-catenin will be phosphorylated by GSK-3β, then ubiquitinated, and ultimately degraded by the protease system at a rapid rate, which will inhibit the physiological function of the downstream signals [49]. When the Wnt protein is activated, it can inhibit the degradation of β-catenin by GSK-3β. In substantial quantities, β-catenin accumulates in the cytoplasm and subsequently translocates to the nucleus, where it binds to the T cell factor/lymphoid enhancing factor (LEF) [50,51]. LEF, which further regulates the expression of Wnt target genes, thus promoting the proliferation of osteoblasts.

Using cell immunofluorescence to measure the expression of Wnt3a and β-catenin. The findings showed that the TD-BNP@DBBM group had considerably greater fluorescence expression than the control and DBBM groups (Fig. 7a and b). The qRT-PCR results showed that the expression levels of Wnt3a and β-catenin were increased, and the expression level of GSK-3β was decreased (Fig. 7c). Western blotting results showed elevated levels of Wnt3a and β-catenin expression (Fig. 7d, Fig. S6).

Additionally, to further confirm that TD promotes bone repair by activating the target pathway, the Wnt signalling pathway inhibitor MASB was used as an inhibitor of this pathway. MSAB is a potent and selective inhibitor of Wnt/β-catenin signalling. MSAB binds to β-catenin and promotes its degradation. Fig. 8a shows the schematic diagram of the activation and inhibition of this pathway. The research consisted of four experimental groups: control, TD, MASB, and TD + MASB. Wnt signalling pathway indicators (Wnt3a and β-catenin) and osteogenesis-related markers (RUNX2, OSX, and OCN) were analysed by PCR and Western blotting. Both approaches showed that MASB significantly decreased Wnt3a and β-catenin expression. Furthermore, the inhibitor MASB significantly reduced osteogenesis-related marker expression, including RUNX2, OSX, and OCN (Fig. 8b–g).

Studies have shown that the osteogenic effects of some bone regeneration materials may be anti-inflammatory effects related, and this study further investigated whether TD-BNP@DBBM has anti-inflammatory effects. Immunofluorescence staining and PCR results showed no significant difference in macrophage polarization (INOS and Arg-1) between TD-BNP@DBBM and control. These findings suggest

that TD-BNP@DBBM did not exhibit significant anti-inflammatory or immunomodulatory effects under the conditions tested (Figs. S7a–d). Although TD-BNP@DBBM does not appear to directly affect immune cell behavior or inflammation, its osteogenic effects are mediated through activation of the Wnt/β-catenin pathway. The lack of an anti-inflammatory effect may limit the application of this material in certain inflammatory situations, but it also highlights its potential for application in situations where immunomodulation is not required.

3.5. TD-BNP@DBBM enhanced bone repair in critical-sized calvarial lesions

To evaluate the osteogenic effect of TD-BNP@DBBM, we created two 5 mm full-layer cranial defect models per rat and filled them with DBBM and TD-BNP@DBBM (Fig. 9a). In the 4th and 8th weeks, microCT (Fig. 9b) showed that TD-BNP@DBBM infilling effectively promoted bone regeneration. As compared to the other two groups, BMD, BV/TV, Tb.th, and Tb.n (Fig. 9c–f) levels were significantly enhanced in the TD-BNP@DBBM group. To study the toxicity of each group to rats, the heart, liver, spleen, lungs, and kidneys of 8W rats from each group were taken for H&E staining, and the results showed no toxicity in any of the groups (Fig. 9g).

The calvarial bone tissue sections underwent histological analysis through H&E and Masson staining. In the TD-BNP@DBBM group, more new bone was observed than in the control and DBBM groups. Furthermore, there were more mature bone tissues at 8 weeks, as opposed to the 4-week mark (Fig. 10a). Immunohistochemical staining was used to evaluate osteogenesis in vivo 8 weeks after implantation of TD-BNP@DBBM in the defect area (Fig. 10b). Increased expression of OCN represented better osteogenesis, and the expression of Wnt3a was detected by immunofluorescence staining (Fig. 10c), which showed an increase in fluorescence expression in the TD-BNP@DBBM group.

To summarize, in vivo experiments were conducted to validate the hypothesis regarding the cellular mechanisms involved. Micro-CT analysis demonstrated that the TD-BNP@DBBM group exhibited more excellent new bone regeneration compared to the other two groups (Fig. 9b). This effect is likely attributed to the enhanced osteogenic differentiation and mineralisation promoted by TD-BNP@DBBM. Most importantly, the newly formed bone in the TD-BNP@DBBM group was denser than the other groups, suggesting that TD released by TD-BNP@DBBM enhanced osteogenesis. We also observed that the TD-BNP@DBBM group formed more new bone tissue on histological staining than the other two groups (Fig. 10a), and immunohistochemistry results showed increased expression of OCN and Wnt3a in the TD-BNP@DBBM group (Fig. 10b and c). Therefore, we concluded that the mechanism by which TD-BNP@DBBM promotes bone reconstruction is by activating the Wnt/β-catenin pathway.

4. Conclusions

This research successfully prepared a novel osteogenic scaffold material using TD-BNP@DBBM. This material not only possesses excellent biocompatibility properties and promotes cell migration but also induces cell differentiation, as well as exhibits excellent bone repair properties by regulating bone regeneration through the Wnt/β-catenin pathway. In vivo experiments showed that in situ implantation of the TD-BNP@DBBM can effectively promote critical bone repair properties. Overall, our results suggest that TD-BNP@DBBM provides a new bioactive material for bone repair and a promising manufacturing method for bone tissue engineering.

CRediT authorship contribution statement

Ya-wen Zhu: Writing – original draft, Methodology, Investigation, Formal analysis, Data curation, Conceptualization. **Yu-wen Wei:** Methodology, Investigation, Formal analysis. **Jing-yi Ma:** Methodology, Investigation. **Wei Chen:** Investigation, Formal analysis. **Zhe Shen:** Methodology, Formal analysis. **Jing Qiu:** Writing – review & editing, Supervision, Resources, Project administration, Funding acquisition, Conceptualization.

Declaration of competing interest

The authors declare that they have no known competing financial interests or personal relationships that could have appeared to influence the work reported in this paper.

Acknowledgements

This work was supported by the National Natural Science Foundation of China (Project Number: 82271003), the Natural Science Foundation of Jiangsu Province (Project Number: BK20241865), and the Jiangsu Province Capability Improvement Project through Science, Technology, and Education-Jiangsu Provincial Research Hospital Cultivation Unit (Project Number: YJXYYJSDW4), Jiangsu Provincial Medical Innovation Center (Project Number: CXZX202227). Figs. 1, 2a, 4a, 8a, 9a and Graphical abstract were created in BioRender.com.

Appendix A. Supplementary data

Supplementary data to this article can be found online at https://doi.org/10.1016/j.mtbio.2025.101730.

Data availability

Data will be made available on request.

References

[1] J. Kulkova, N. Moritz, E.O. Suokas, N. Strandberg, K.A. Leino, T.T. Laitio, H.T. Aro, Osteointegration of PLGA implants with nanostructured or microsized β-TCP particles in a minipig model, J. Mech. Behav. Biomed. Mater. 40 (2014) 190–200.
[2] Y. Liu, D. Luo, T. Wang, Hierarchical structures of bone and bioinspired bone tissue engineering, Small 12 (2016) 4611–4632.
[3] Q. Yuan, B. Bao, M. Li, L. Li, X. Zhang, Y. Tang, Bioactive conjugated polymer-based biodegradable 3D bionic scaffolds for facilitating bone defect repair, Adv. Healthcare Mater. 13 (2024) 2302818.
[4] X. Zhou, Y. Qian, L. Chen, T. Li, X. Sun, X. Ma, J. Wang, C. He, Flowerbed-Inspired biomimetic scaffold with rapid internal tissue infiltration and vascularization capacity for bone repair, ACS Nano 17 (2023) 5140–5156.
[5] J. Ng, K. Spiller, J. Bernhard, G. Vunjak-Novakovic, Biomimetic approaches for bone tissue engineering, Tissue Engineering Part B: Reviews 23 (2017) 480–493.
[6] C. Li, J. Wang, Y. Niu, H. Zhang, H. Ouyang, G. Zhang, Y. Fu, Baicalin nanocomplexes with an *in situ* -forming biomimetic gel implant for repair of calvarial bone defects *via* localized sclerostin inhibition, ACS Appl. Mater. Interfaces 15 (2023) 9044–9057.
[7] X. Chen, H. Wang, Y. Wang, Y. Shi, Z. Wang, Enhanced osteogenesis by addition of cancellous bone chips at xenogenic bone augmentation: in vitro and in vivo experiments, Clinical Oral Implants Res 34 (2023) 42–55.
[8] D.S. Thoma, A. Kruse, C. Ghayor, R.E. Jung, F.E. Weber, Bone augmentation using a synthetic hydroxyapatite/silica oxide-based and a xenogenic hydroxyapatite-based bone substitute materials with and without recombinant human bone morphogenetic protein-2, Clinical Oral Implants Res 26 (2015) 592–598.
[9] L. Autelitano, M. Meazzini, Alveolar Cleft Reconstruction with Vomerine Bone: Two Surgical Procedures in One Step: a Case Series, Plastic and Aesthetic Research, 2023.
[10] Y. Lei, Q. Zhang, G. Kuang, X. Wang, Q. Fan, F. Ye, Functional biomaterials for osteoarthritis treatment: from research to application, Smart Medicine 1 (2022) e20220014.
[11] J.-W. Choi, Y.-C. Kim, Asian facial recontouring surgery, Plast Aesthet Res 10 (2023) 59.
[12] Y. Xu, Q. Saiding, X. Zhou, J. Wang, W. Cui, X. Chen, Electrospun fiber-based immune engineering in regenerative medicine, Smart Medicine 3 (2024) e20230034.
[13] M.T. Howard, S. Wang, A.G. Berger, J.R. Martin, S. Jalili-Firoozinezhad, R. F. Padera, P.T. Hammond, Sustained release of BMP-2 using self-assembled layer-by-layer film-coated implants enhances bone regeneration over burst release, Biomaterials 288 (2022) 121721.
[14] P. Xia, S. Wang, Z. Qi, W. Zhang, Y. Sun, BMP-2-releasing gelatin microspheres/PLGA scaffolds for bone repairment of X-ray-radiated rabbit radius defects, Artificial Cells, Nanomedicine, and Biotechnology 47 (2019) 1662–1673.

[15] K. Sun, H. Lin, Y. Tang, S. Xiang, J. Xue, W. Yin, J. Tan, H. Peng, P.G. Alexander, R. S. Tuan, B. Wang, Injectable *BMP-2* gene-activated scaffold for the repair of cranial bone defect in mice, Stem Cells Translational Medicine 9 (2020) 1631–1642.
[16] Y. Xu, Y. Jiang, B. Jia, Y. Wang, T. Li, Icariin stimulates osteogenesis and suppresses adipogenesis of human bone mesenchymal stem cells via miR-23a-mediated activation of the Wnt/β-catenin signaling pathway, Phytomedicine 85 (2021) 153485.
[17] S. Yang, G. Ni, M. Xia, H. Li, Z. Gao, Mussel inspired multifunctional bovine serum albumin (BSA) coatings loaded with Baicalein (Bai) to enhance osteogenesis and resist oxidative stress for potential application on implant, Int. J. Biol. Macromol. 229 (2023) 752–765.
[18] H. Lin, X. Wang, Z. Li, M. Huang, J. Feng, H. Chen, J. Gao, Y. Feng, J. Wu, S. Tang, R. Zhou, Y. Ren, F. Huang, Z. Jiang, Total flavonoids of *Rhizoma drynariae* promote angiogenesis and osteogenesis in bone defects, Phytother Res. 36 (2022) 3584–3600.
[19] S. Sanchez-Casanova, F.M. Martin-Saavedra, C. Escudero-Duch, M.I. Falguera Uceda, M. Prieto, M. Arruebo, P. Acebo, M.L. Fabiilli, R.T. Franceschi, N. Vilaboa, Local delivery of bone morphogenetic protein-2 from near infrared-responsive hydrogels for bone tissue regeneration, Biomaterials 241 (2020) 119909.
[20] L. Bai, G. Tao, M. Feng, Y. Xie, S. Cai, S. Peng, J. Xiao, Hydrogel drug delivery systems for bone regeneration, Pharmaceutics 15 (2023) 1334.
[21] Y. Li, C. Xu, C. Lei, The delivery and activation of growth factors using nanomaterials for bone repair, Pharmaceutics 15 (2023) 1017.
[22] for the ARGO investigators, S. Lovestone, M. Boada, B. Dubois, M. Hüll, J.O. Rinne, H.-J. Huppertz, M. Calero, M.V. Andrés, B. Gómez-Carrillo, T. León, T. Del Ser, A phase II trial of tideglusib in alzheimer's disease, JAD 45 (2015) 75–88.
[23] C. Kornsuthisopon, K.A. Tompkins, T. Osathanon, Tideglusib enhances odontogenic differentiation in human dental pulp stem cells *in vitro*, Int. Endod. J. 56 (2023) 369–384.
[24] R. Osorio, F.J. Rodríguez-Lozano, M. Toledano, M. Toledano-Osorio, D. García-Bernal, L. Murcia, S. López-García, Mitigating lipopolysaccharide-induced impairment in human dental pulp stem cells with tideglusib-doped nanoparticles: enhancing osteogenic differentiation and mineralization, Dent. Mater. (2024) S010956412400215X.
[25] D. Atila, C.-Y. Chen, C.-P. Lin, Y.-L. Lee, V. Hasirci, A. Tezcaner, F.-H. Lin, In vitro evaluation of injectable Tideglusib-loaded hyaluronic acid hydrogels incorporated with Rg1-loaded chitosan microspheres for vital pulp regeneration, Carbohydr. Polym. 278 (2022) 118976.
[26] R. Khandelia, T. Hodgkinson, D. Crean, D.F. Brougham, D. Scholz, H. Ibrahim, S. J. Quinn, B.J. Rodriguez, O.D. Kennedy, J.M. O'Byrne, D.J. Brayden, Reproducible synthesis of biocompatible albumin nanoparticles designed for intra-articular administration of celecoxib to treat osteoarthritis, ACS Appl. Mater. Interfaces 16 (2024) 14633–14644.
[27] S. Ortelli, A.L. Costa, I. Zanoni, M. Blosi, O. Geiss, I. Bianchi, D. Mehn, F. Fumagalli, G. Ceccone, G. Guerrini, L. Calzolai, TiO2@BSA nano-composites investigated through orthogonal multi-techniques characterization platform, Colloids Surf. B Biointerfaces 207 (2021) 112037.
[28] Z. Yang, W. He, H. Zheng, J. Wei, P. Liu, W. Zhu, L. Lin, L. Zhang, C. Yi, Z. Xu, J. Ren, One-pot synthesis of albumin-gadolinium stabilized polypyrrole nanotheranostic agent for magnetic resonance imaging guided photothermal therapy, Biomaterials 161 (2018) 1–10.
[29] W. Li, Y. Wang, W. Li, L. Liu, X. Wang, S. Song, Nanoparticle-containing hyaluronate solution for improved lubrication of orthopedic ceramics, Polymers 14 (2022) 3485.
[30] A. Chua, T.-T. Tran, S. Pu, J.-W. Park, K. Hadinoto, Lyophilization of curcumin–albumin nanoplex with sucrose as cryoprotectant: aqueous reconstitution, dissolution, kinetic solubility, and physicochemical stability, IJMS 23 (2022) 11731.
[31] D. Guo, H. Liu, S. Zhao, X. Lu, H. Wan, Y. Zhao, X. Liang, A. Zhang, M. Wu, Z. Xiao, N. Hu, Z. Li, D. Xie, Synergistic rheumatoid arthritis therapy by interrupting the detrimental feedback loop to orchestrate hypoxia M1 macrophage polarization using an enzyme-catalyzed nanoplatform, Bioact. Mater. 41 (2024) 221–238.
[32] P. Duan, L.F. Bonewald, The role of the wnt/β-catenin signaling pathway in formation and maintenance of bone and teeth, Int. J. Biochem. Cell Biol. 77 (2016) 23–29.
[33] W. Chen, H. Lu, W. Yu, L. Huang, M. Bian, N. Wang, X. Xiang, G. Mo, C. Zhang, Y. Li, L. Jiang, J. Zhang, Magnesium-impregnated membrane promotes bone regeneration in rat skull defect by N-linked glycosylation of SPARC via MagT1, Adv. Healthcare Mater. 14 (2025) 2402705.
[34] H. Huang, L. Xiao, L. Fang, M. Lei, Z. Liu, S. Gao, Q. Lei, J. Lei, R. Wei, Y. Lei, L. Xue, Z. Geng, L. Cai, F. Yan, Static topographical cue combined with dynamic fluid stimulation enhances the macrophage extracellular vesicle yield and therapeutic potential for bone defects, ACS Nano (2025) 4c15201 acsnano.
[35] T. Komori, Regulation of proliferation, differentiation and functions of osteoblasts by Runx2, IJMS 20 (2019) 1694.
[36] A. Narayanan, N. Srinaath, M. Rohini, N. Selvamurugan, Regulation of Runx2 by MicroRNAs in osteoblast differentiation, Life Sci. 232 (2019) 116676.
[37] M. Korostishevsky, I. Malkin, S. Trofimov, Y. Pei, H.-W. Deng, G. Livshits, Significant association between body composition phenotypes and the osteocalcin genomic region in normative human population, Bone 51 (2012) 688–694.
[38] A. Neve, A. Corrado, F.P. Cantatore, Osteocalcin: skeletal and extra-skeletal effects, J. Cell. Physiol. 228 (2013) 1149–1153.
[39] M.-K. Choo, H. Yeo, M. Zayzafoon, NFATc1 mediates HDAC-dependent transcriptional repression of osteocalcin expression during osteoblast differentiation, Bone 45 (2009) 579–589.
[40] Z. Cheng, T. Han, J. Yao, K. Wang, X. Dong, F. Yu, H. Huang, M. Han, Q. Liao, S. He, W. Lyu, Q. Li, Targeting glycogen synthase kinase-3β for Alzheimer's disease: recent advances and future Prospects, Eur. J. Med. Chem. 265 (2024) 116065.
[41] Y. Dong, J. Lu, S. Zhang, L. Chen, J. Wen, F. Wang, Y. Mao, L. Li, J. Zhang, S. Liao, L. Dong, Design, synthesis and bioevaluation of 1,2,4-thiadiazolidine-3,5-dione derivatives as potential GSK-3β inhibitors for the treatment of Alzheimer's disease, Bioorg. Chem. 134 (2023) 106446.
[42] T. Pozner, A. Schray, M. Regensburger, D.C. Lie, U. Schlötzer-Schrehardt, J. Winkler, S. Turan, B. Winner, Tideglusib rescues neurite pathology of SPG11 iPSC derived cortical neurons, Front. Neurosci. 12 (2018) 914.
[43] J. Sun, H. Zhao, C. Shen, S. Li, W. Zhang, J. Ma, Z. Li, M. Zhang, J. Yang, Tideglusib promotes wound healing in aged skin by activating PI3K/Akt pathway, Stem Cell Res. Ther. 13 (2022) 269.
[44] H. Zhang, J. Wang, F. Deng, E. Huang, Z. Yan, Z. Wang, Y. Deng, Q. Zhang, Z. Zhang, J. Ye, M. Qiao, R. Li, J. Wang, Q. Wei, G. Zhou, H.H. Luu, R.C. Haydon, T.-C. He, F. Deng, Canonical Wnt signaling acts synergistically on BMP9-induced osteo/odontoblastic differentiation of stem cells of dental apical papilla (SCAPs), Biomaterials 39 (2015) 145–154.
[45] J. Shen, Y. Sun, X. Liu, Y. Zhu, B. Bao, T. Gao, Y. Chai, J. Xu, X. Zheng, EGFL6 regulates angiogenesis and osteogenesis in distraction osteogenesis via Wnt/β-catenin signaling, Stem Cell Res. Ther. 12 (2021) 415.
[46] E. Vincan (Ed.), Wnt Signaling, Humana Press, Totowa, NJ, 2008.
[47] R.T. Moon, N.R. Gough, Beyond canonical: the Wnt and β-catenin story, Sci. Signal. 9 (2016).
[48] J. Liu, Q. Xiao, J. Xiao, C. Niu, Y. Li, X. Zhang, Z. Zhou, G. Shu, G. Yin, Wnt/β-catenin signalling: function, biological mechanisms, and therapeutic opportunities, Sig Transduct Target Ther 7 (2022) 3.
[49] R. Nusse, H. Clevers, Wnt/β-Catenin signaling, disease, and emerging therapeutic modalities, Cell 169 (2017) 985–999.
[50] N.C. Inestrosa, C. Montecinos-Oliva, M. Fuenzalida, Wnt signaling: role in alzheimer disease and schizophrenia, J. Neuroimmune Pharmacol. 7 (2012) 788–807.
[51] D. Wu, W. Pan, GSK3: a multifaceted kinase in Wnt signaling, Trends Biochem. Sci. 35 (2010) 161–168.